Effect of Mono-Vacant Defects on the Adsorption Properties of Deep Eutectic Solvents onto Hexagonal Boron-Nitride Nanoflakes

Mehdi Shakourian-Fard[a*], S. Maryamdokht Taimoory[b, c], Hamid Reza Ghenaatian[d], Ganesh Kamath[e], John F. Trant[b*]

[a] Department of Chemical Engineering, Birjand University of Technology, Birjand, P.O. Box 97175/569, Iran.
[b] University of Windsor, Department of Chemistry and Biochemistry, 401 Sunset Ave. Windsor, Ontario, N9B 3P4, Canada.
[c] University of Michigan, Department of Chemistry, 930 North University Ave. Ann Arbor, MI 48109-1055, USA.
[d] Department of Physics, Jahrom University, Jahrom, P.O. Box 74135-111, Iran.
[e] Dalzierfiver LLC, 3500 Carlfied St, EL Sobrante, CA 94803, USA.

*Corresponding authors:

E-mail: shakourian@birjandut.ac.ir

E-mail: j.trant@uwindsor.ca

Abstract:

Hexagonal boron nitride is a promising material for a variety of electronic, optical, and material science applications. Both the synthesis of the material through exfoliation, and its various applications almost inevitably require its solvation. Deep eutectic solvents (DES) are extremely useful solvents for these types of applications due to their non-volatility, inflammability, biocompatibility, and reasonable cost. There are many different deep eutectic solvents available, and their suitability for any given application is particularly dependent on the specific of their structure. DES have been examined computationally for use with boron nitride, but these calculations use idealized, perfect boron nitride sheets instead of the more realistic, defect-containing systems. In this report, we investigated four DESs with two experimentally observed defective boron nitride, one with a single boron vacancy, the other with a single nitrogen vacancy. All DESs bound with higher affinity to the defective boron nitride than to the pristine surface. Charge transfer was minimal in all cases although the surfaces tended to donate electron density to the solvents. The interactions between the solvents and the surfaces are primarily non-covalent although in several cases natural bond order analysis indicates a partial covalent interaction that helps explain the higher-than-expected affinity for particular DES. The DESs have little effect on the predicted optical behaviour of the pristine boron nitride but do significantly change the adsorption spectrum of the defective boron nitride nanoflakes; the effect on bulk material might be limited. Together these results suggest that the choice of DES can either be made to limit any effect on the properties of the material (urea-choline chloride) or to affect the optical and electronic nature of the material (benzoic acid-choline chloride).

Keywords: Hexagonal boron-nitride, Structural defects, Deep eutectic solvents, Noncovalent interaction, DFT

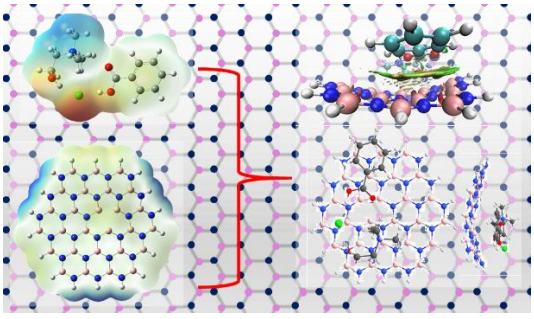

1. Introduction

Non-traditional solvents, such as ionic liquids and deep eutectic solvents are being increasingly used as the fluid component of new devices assembled at the nanoscale, including electronics, and hydrogen storage. This is because they have outstanding operating temperature range and are non-volatile.[1] Deep eutectic solvents, mixtures of materials that are not, in themselves, liquids, but when mixed together in precise ratios become admittedly viscous liquids at near room temperatures, are particularly promising due to their safety profile.[2] The archetype is the 2:1 mixture of urea (melting point of 133 ºC) and choline chloride (m.p. of 302 ºC), forms a new mixture with a melting point of 12 ºC. This remarkable drop in crystallinity results from the remarkably strong, normally hydrogen bond, interactions between the chloride anion of one partner and the hydrogen bond donor of the other; this prevents phase separation of the components, inhibiting the crystallization of either one separately. Furthermore, as these are normally highly flexible in the orientation of the interaction, no repeating crystalline structure generally arises, helping to further lower the melting point.

A particular application of DES is for providing the medium for the synthesis of functional materials like graphene nanosheets.[3] To help determine ideal conditions, DES have been studied using a variety of different computational methods, either alone to understand the liquid phase,[4] or in the presence of idealized defect-free nanosheet surfaces.[5] In the latter example, the perfection of the surface limits entropic considerations and the second solvation layer of Reline (the trade name of this 2:1 mixture of urea and choline chloride) can adopt the conformation of bulk solvent. This is clearly a wonderful combination of material and solvent. The limitation of this approach is that it considers the 2-D nanosheet to be perfect; however, defects are nearly universal. We recently discussed how defects in graphene sheets disrupt deep eutectic solvent interactions with the surface.[6] In general, we found that the presence of defects increases the adsorption energy of the DES; simply put, the imperfections provide asymmetrical “anchor points” that disrupt the regularity of the electron density surface of the material. Exploiting this allows the DES to form stronger interactions than with the surface than it can with the pristine version of the material. These defects also affect the preferred binding mode, and even orientation in some cases, of the DES-nanosheet interaction.

Along with graphene, boron nitride has emerged as an extremely promising nanomaterial.[7] It shows far better potential, natively, for hydrogen storage than pure carbon-based materials;

native boron nitride nanotubes can store 2.6 wt % hydrogen at room temperature,[8] far higher than the 0.1-0.5% observed for native carbon nanotubes.[9] This can be increased far further through doping the material with metals.[7b] Our recent work in computationally examining doped boron-nitride as a hydrogen-storage material looked at the different topologies available in boron nitride nanotubes and their potential for changing hydrogen capacity as a function of aluminum doping.[10] However we did not consider the defects, nor has any other computational study into boron nitride doping for hydrogen storage. However, before examining that challenge, we wanted to investigate the interaction of DES with the defects that occur in boron nitride during preparation. In this study, we examine the effects of two defects introduced into hexagonal boron nitride nanoflakes (**h-BNNF**): a single boron vacancy (**B_{vac}-h-BNNF**) and a single nitrogen vacancy (**N_{vac}-h-BNNF**). We recognize that these are not necessarily the only point-imperfections in the sheets: Stone-Wales defects (as observed in graphene) should be possible, although they have not yet been experimentally observed, as should unusual insertion or sheet-interstitial binding depending on the synthetic strategy.[7a] Unlike these, at this time, theoretical defects, point vacancy defects have been clearly observed—the single boron vacancy **B_{vac}-h-BNNF** is relatively appears 110,000 times per square micrometer, while **N_{vac}-h-BNNF** defects are far rarer 4,700 times over the same area.[11] These defects have been predicted to have significant effects on the electronics of the system.[12] Other common defects are also certainly possible and have been observed, including substitutions within the 2-D structure itself (as distinct from chemoabsorbed dopant metals added after synthesis) due to impurities during synthesis,[13] and larger geometric vacancies where entire groups of atoms are missing from the sheet, although curiously the geometry of the missing component is highly temperature dependent.[14] Although important, these two types of defects are far more variable and the possible models to be examined rapidly exceeds the number viable for any preliminary study. Consequently, we have restricted our examination to the two single point vacancies **B_{vac}-h-BNNF** and **N_{vac}-h-BNNF** and the comparison of their interactions with DES to idealized **h-BNNF**.

This study, like our previous graphene analysis, is restricted to four common but functionally diverse DES (Figure 1). All use choline chloride (**ChCl**) as the hydrogen bond acceptor (HBA); choline chloride's safety, cost, functionality, and availability make it difficult for any other salt to compete and it is by far the most common HBA used in DES. We examine four different hydrogen bond donors to generate the molecular complexity: urea (**U**), glycerol (**Gly**),

ethylene glycol (**EG**), and benzoic acid (**BA**). Each offers a unique challenge: urea is the standard system with the four potentially strong H-bonds generatable from the nitrogenous protons. The comparably acidic benzoic acid makes for a very strong hydrogen bond donor, and the aromatic nature of the phenyl ring can favour π-interactions with the sheet. Ethylene glycol and glycerol differ by the number of hydrogen bond donors per molecule. Together these four materials allow us to sample the chemical space.

In this study, we examine these systems using the M06-2X functional and cc-pVDZ basis set have already been used in the literature to investigate the interaction of graphene,[15] defective graphene,[16] nitrogen-doped graphene,[17] hexagonal boron nitride,[18] and defective hexagonal boron nitride [19] surfaces with ionic liquids, and graphene and defective graphene surfaces with deep eutectic solvents.[6] This level of theory has been useful for compensating for the longer range non-covalent interactions present in these systems; the lack of heavier atoms in the systems does certainly simplify the calculations, allowing us to use the smaller basis set.[20]

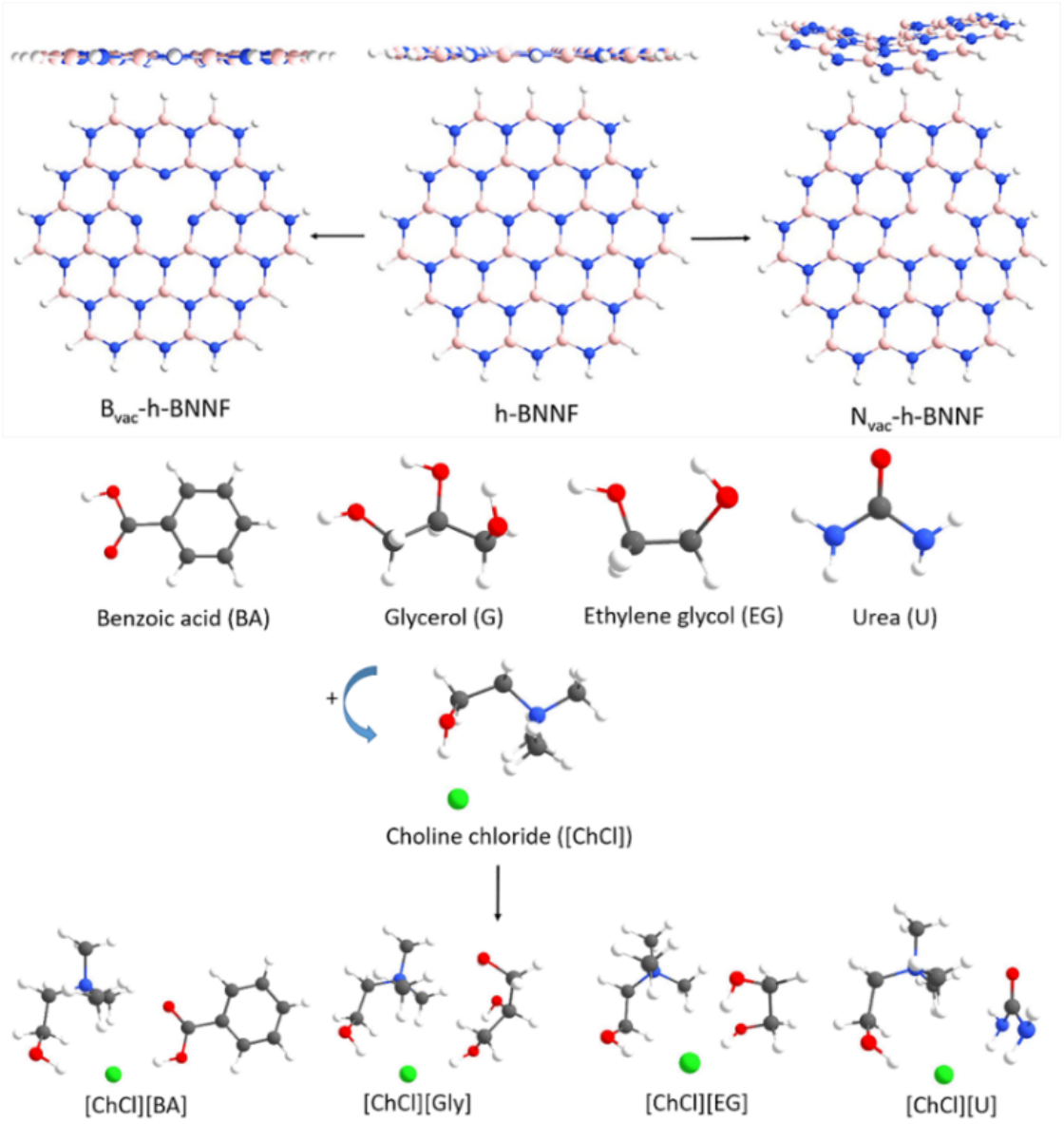

Figure 1. The most stable geometries of the **h-BNNF**, **B_{vac}-h-BNNF** and **N_{vac}-h-BNNF** surfaces (both top down and along the plane); HBA (Choline chloride (**ChCl**)); HBDs (Benzoic acid (**BA**), Glycerol (**Gly**), Ethylene glycol (**EG**), and Urea (**U**)); and DESs (**[ChCl][BA]**, **[ChCl][Gly]**, **[ChCl][EG]**, **[ChCl][U]**).

2. Computational details

Density functional theory (DFT) calculations were carried out using the M06-2X functional,[21] with D3 dispersion corrections according Grimme's scheme[22] employing Dunning's correlation consistent polarized valence double zeta basis set (cc-pVDZ).

The full geometry optimization, optical properties, and electronic properties on the adsorption process of deep eutectic solvents (DESs) on the hexagonal boron-nitride nanoflake ($B_{27}N_{27}H_{18}$ (**h-BNNF**)) and **h-BNNF** containing boron and nitrogen vacancies ($B_{26}N_{27}H_{18}$ (**B_{vac}-h-BNNF**) and $B_{27}N_{26}H_{18}$ (**N_{vac}-h-BNNF**), respectively) were studied using the Gaussian 09 D.01 suite of programs.[23] To characterize the stationary points and calculation of zero-point vibrational energy (ZPVE) as well as thermochemical quantities, vibrational frequencies were calculated at the M06-2X/cc-pVDZ level of theory. Vibrational frequency analysis indicated that all the DESs, DES∩surface complexes, and their individual constituent components correspond to energetic minima and not imaginary frequencies. The **h-BNNF** model was used as the pristine structure for generating the **B_{vac}-h-BNNF** and **N_{vac}-h-BNNF** models. The **B_{vac}-h-BNNF** and **N_{vac}-h-BNNF** models were built by removing boron (B) and nitrogen (N) atoms from the pristine **h-BNNF** model, respectively. These models were previously used in literature to investigate the interaction of defective boron nitride with ionic liquids.[18-19]

The adsorption energy (E_{ads}) values of the **[ChCl][U]**, **[ChCl][Gly]**, **[ChCl][EG]**, and **[ChCl][BA]** deep eutectic solvents on the **h-BNNF**, **B_{vac}-h-BNNF**, and **N_{vac}-h-BNNF** surfaces were calculated using the following equation:

$$E_{ads} = E_{(DES\cap surface)} - [E_{(DES)} + E_{(surface)}] + BSSE \quad (1)$$

where $E_{(DES\cap surface)}$, $E_{(DES)}$ and $E_{(surface)}$ stand for the total energy of the DES∩surface complexes, DESs, and the surfaces (**h-BNNF**, **B_{vac}-h-BNNF** or **N_{vac}-h-BNNF**), respectively. The BSSE term stands for the basis set superposition error (BSSE), which was taken into account using the Boys-Bernardi counterpoise method.[24] In addition to adsorption energy, enthalpy of adsorption (ΔH_{ads}) and free energy of adsorption (ΔG_{ads}) for adsorption of DESs on the surfaces were calculated at 298.15 K according to the following equations:

$$\Delta H_{ads} = H_{(DES\cap surface)} - [H_{(DES)} + H_{(surface)}] \quad (2)$$

$$\Delta G_{ads} = G_{(DES\cap surface)} - [G_{(DES)} + G_{(surface)}] \quad (3)$$

In these equations, $H/G_{(DES\cap surface)}$, $H/G_{(DES)}$, and $H/G_{(surface)}$ are the enthalpy/free energy of the DES∩surface complexes, DESs, and the surfaces, respectively.

The charge transfer values between the DESs and the surfaces were calculated using the ChelpG charge analysis.[25] The electrostatic potential (ESP) maps were calculated at the M06-2X/cc-pVDZ level of theory. Topological properties of electron charge density including electron

density, ρ(r), Laplacian of electron density, $\nabla^2\rho(r)$, kinetic energy density, G(r), potential energy density, V(r), and total energy density, H(r) (H(r) = G(r) + V(r)),[26] were also calculated at the same level of theory using the AIM2000 program package.[27] The Multiwfn 3.7 program was used to analyze the noncovalent interactions (NCIs) responsible for adsorption of DESs on the surfaces.[28] Then, the reduced density gradient (RDG) isosurface versus the sign(λ_2)ρ was plotted for the DES∩surface complexes using the VMD 1.9.3 program.[29] Global molecular descriptors such as HOMO-LUMO energy gap ($E_g = E_{LUMO} - E_{HOMO}$) and chemical hardness ($\eta = (E_{LUMO} - E_{HOMO})/2$) of the surfaces and DES∩surface complexes were obtained from the energies of the highest occupied molecule orbital (HOMO) and the lowest unoccupied molecular orbital (LUMO).[30]

Time dependent DFT (TDDFT) calculations at the M06-2X/cc-pVDZ level of theory have been used to simulate UV/Vis absorption spectra of the surfaces and DES∩surface complexes. In the TDDFT calculations, ten excited states were considered for each surface and DES∩surface complex. In order to realize the nature of electron excitation in the surfaces and DES∩surface complexes, the excited-state properties and the fragment transition density matrix (FTDM) maps were calculated at the same level of theory.

3. Results and discussion

3.1. Electrostatic potential (ESP) maps and the most stable geometry of ChCl, DESs and DES∩surface complexes

The electrostatic potential (ESP) map is a local physical property related to electron density at various points in three-dimensional space allowing us to visualize local negative and positive electrostatic potential in a system and to understand the intermolecular interactions between polar species. It is a very useful descriptor in identifying the most reactive sites in molecules and in suggesting electrophilic and nucleophilic loci for chemical reactions.[31] In the ESP maps, the negative electrostatic potentials (electron-rich regions) and positive electrostatic potentials (electron-deficient regions) are shown in red and blue respectively. Regions with zero electrostatic potential are shown in green. The most stable geometries of the DESs formed by mixing HBA **ChCl** with the four separate HBDs (Benzoic acid (**BA**), Glycerol (**Gly**), Ethylene glycol (**EG**), and Urea (**U**)) were calculated at the M06-2X/cc-pVDZ level of theory. The ESP maps of **[Ch]**$^+$ cation, **[Cl]**$^-$ anion, **ChCl** and the HBDs and provided as Figure S1.

As seen from the ESP of the **[Ch]**$^+$ cation, all regions around the **[Ch]**$^+$ cation have the expected positive electrostatic potential (blue). The ESP of **[Ch]**$^+$ cation shows that the positive charge density is localized at the N atom, O-H bond and C-H bonds of the cation. A uniform distribution of negative charge is seen over the **[Cl]**$^-$ anion. This standard electrostatic ion-pair attraction holds the salt together. Then, multiple starting configurations with various relative positionings of the ion pair were optimized at the M06-2X/cc-pVDZ level of theory and sorted according to their energy from the lowest energy to the highest energy. The geometry with the lowest energy was identified as the most stable geometry of **ChCl** and shown in Figure 1, this is consistent with the same geometry previously found by us.[6] In this optimized geometry, the **[Ch]**$^+$ cation interacts with **[Cl]**$^-$ anion through O-H···[Cl]$^-$ (2.106 Å) and C-H···[Cl]$^-$ (2.387 Å) hydrogen bond (H-bond) interactions.

With this substructure obtained, the most stable geometry of the complete DESs for adsorption was calculated. The ESP maps of **ChCl** with the HBDs were calculated at the same level of theory (Figure S1). The chloride anion and the O atom in **ChCl** along with the O atoms in the HBDs have a negative electrostatic potential, while the N atom and the C-H bonds in the **[Ch]**$^+$ cation as well as the C-H, N-H, and O-H bonds in the HBDs have a positive electrostatic potential (blue). Again, the complexes were optimized from various starting conformations at the M06-2X/cc-pVDZ level of theory to identify the geometries with the lowest energy value for each of **[ChCl][BA]**, **[ChCl][Gly]**, **[ChCl][EG]**, and **[ChCl][U]** (Figure 1).

As seen from Figure 1, the geometry of **ChCl** remains generally unchanged upon interaction with the HBD molecules and new favorable H-bond interactions are formed between the **[Cl]**$^-$ anion in the **ChCl** and the O-H and N-H bonds in the HBD components. This is consistent with the results observed in the literature.[32]

In order to identify all relevant interacting modes of the DESs with the **h-BNNF**, **B$_{vac}$-h-BNNF** and **N$_{vac}$-h-BNNF** surfaces, many different starting configurations were considered based on the ESP maps of the DESs and the surfaces. As seen from Figure S1, the ESPs of the surfaces are different at the Boron (B)-vacancy and Nitrogen (N)-vacancy sites created in the **B$_{vac}$-h-BNNF** and **N$_{vac}$-h-BNNF** surfaces, respectively; a more negative electrostatic potential is seen at the B-vacancy site than N-vacancy site. This renders **B$_{vac}$-h-BNNF** more attractive than the **N$_{vac}$-h-BNNF** surface for the positive electrostatic potential components of the DES. The starting configurations were built by putting the DES at an average vertical distance of 2.7 Å from the

center of the **h-BNNF** surface and likewise the same distance directly above the B-vacancy and N-vacancy sites in the **B_{vac}-h-BNNF** and **N_{vac}-h-BNNF** surfaces, respectively. Then, the starting configurations for interaction of each of the DESs with the surfaces were optimized at the M06-2X/cc-pVDZ level and sorted according to their energy from the lowest energy to the highest energy, notably many of the starting configurations all converged towards the same lowest energy conformation. Finally, the DES∩surface optimized configurations with the lowest energy were identified as the most stable geometry for interaction of each DES with the surfaces (Figure 2, Figure S2).

3.1. Adsorption of DESs on the h-BNNF, B_{vac}-h-BNNF, and N_{vac}-h-BNNF surfaces

The pristine boron nitride surface is, of course, symmetric. Interactions between the DES and the surface is mediated by induced dipoles on the surface, but these are, of course, of limited magnitude. It is consequently unsurprising that the pattern-breaking induced by the defective surfaces increases interactions. In all cases, the adsorption strength follows the pattern: **DES∩B_{vac}-h-BNNF**>> **DES∩N_{vac}-h-BNNF**> **DES∩h-BNNF**. The defects increase binding by 29.1 to 33.3 kcal/mol for the boron vacancy with the exception of benzoic acid which sees a far more modest improvement of only 12.8 kcal/mol; and 0.3 to 1.8 kcal/mol for the nitrogen vacancy with the exception of the ethylene glycol DES that improves affinity to 10.8 kcal/mol (Table 1).

Table 1. The calculated adsorption energy (E_{ads} in kcal/mol), enthalpy of adsorption (ΔH_{ads} in kcal/mol), free energy of adsorption (ΔG_{ads} in kcal/mol) and charge transfer (Q_{CT} in e) of the DES∩surface complexes.

Structure	E_{ads}	ΔH_{ads}	ΔG_{ads}	[a]Q_{CT}
[ChCl][U]∩h-BNNF	-15.3	-15.2	-1.0	0.053
[ChCl][Gly]∩h-BNNF	-17.1	-19.0	-5.8	0.026
[ChCl][EG]∩h-BNNF	-14.1	-17.1	-2.6	0.0042
[ChCl][BA]∩h-BNNF	-19.9	-23.2	-8.3	-0.034
[ChCl][U]∩B_{vac}-h-BNNF	-48.6	-52.0	-36.2	-0.068
[ChCl][Gly]∩B_{vac}-h-BNNF	-46.2	-46.8	-31.4	0.063
[ChCl][EG]∩B_{vac}-h-BNNF	-44.0	-45.7	-30.5	0.085
[ChCl][BA]∩B_{vac}-h-BNNF	-32.7	-36.7	-25.1	-0.029
[ChCl][U]∩N_{vac}-h-BNNF	-17.1	-19.8	-7.8	0.077
[ChCl][Gly]∩N_{vac}-h-BNNF	-17.4	-19.5	-6.2	0.032
[ChCl][EG]∩N_{vac}-h-BNNF	-24.8	-28.7	-13.0	-0.24
[ChCl][BA]∩N_{vac}-h-BNNF	-21.5	-24.7	-10.4	0.027

[a] Q_{CT} is obtained by calculation of the ChelpG charge on the surfaces in the DES∩surface complexes.

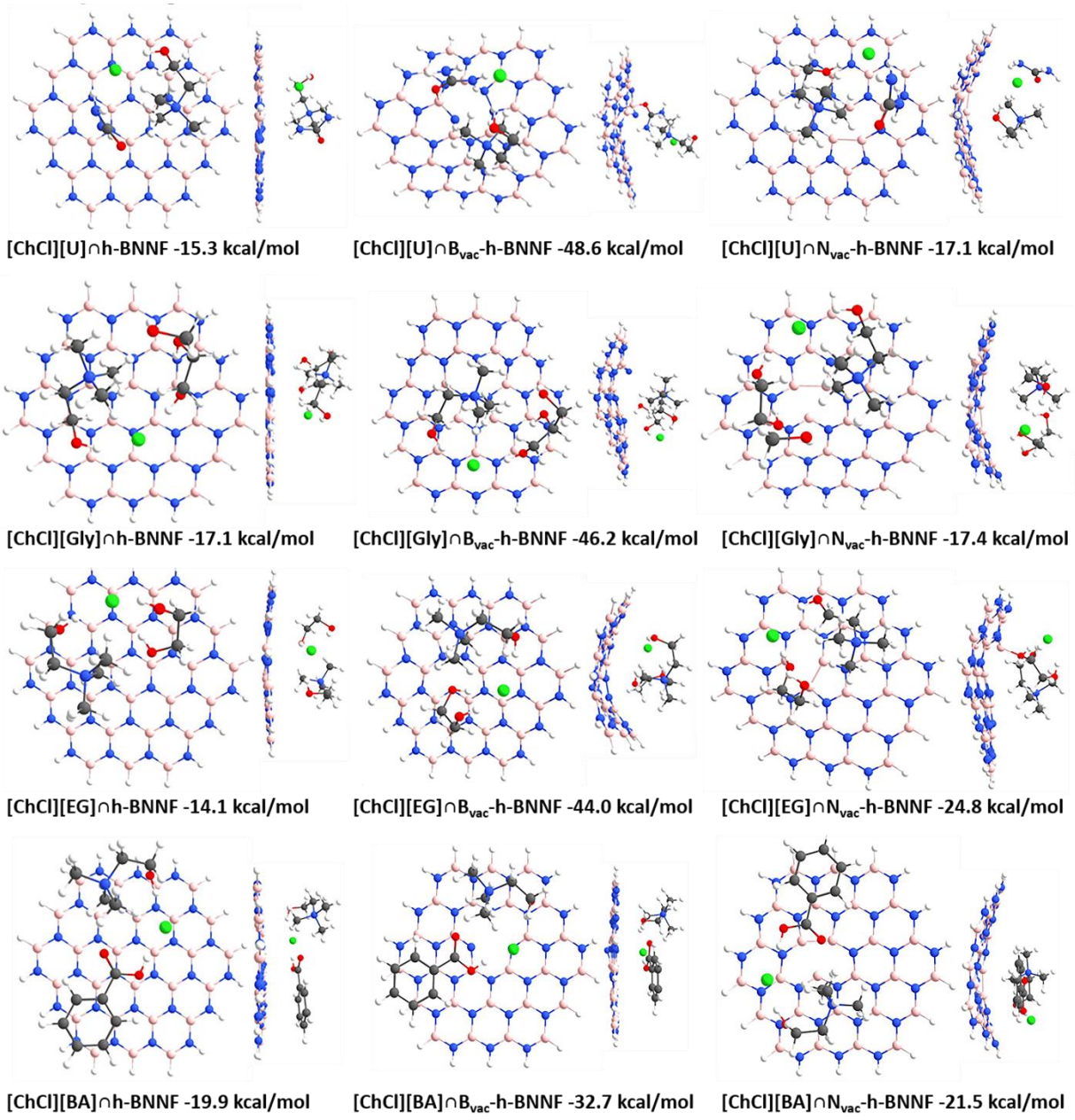

Figure 2. Optimized structures of the DES interacting with the boron nitride surfaces with both a top-down and side-on view. Non-bonding interaction analyses are provided as Figure S2. The numerical values represent the energy of adsorption.

All energies of absorption are strongly negative indicating all interactions are favourable. The structures provide some insight into why the exceptions occur. In the case of the weakly binding **[ChCl][BA]∩B$_{vac}$-h-BNNF**, the surface barely distorts towards the DES. In all other cases, the nanoflake seeks to bend towards the solvent increasing the binding surface. This isn't the case here, and it decreases the interaction surface, so of course this also decreases the energy of adsorption. The other outlier is the **[ChCl][EG]∩N$_{vac}$-h-BNNF**. This is the only case of all examined where the DES adopts a perpendicular form: one of the hydroxyls of ethylene glycol points directly towards the hole of the vacancy, and interaction missing from all of the other DES. This could explain the improved affinity. The enthalpy of adsorption (ΔH_{ads}) and free energy of adsorption (ΔG_{ads}) values for the formation of DES∩surface complexes were also calculated at the M06-2X/cc-pVDZ level of theory. The negative sign of ΔH_{ads} and ΔG_{ads} values suggests that the formation of DES∩surface complexes is an exothermic-spontaneous reaction, and these values follow the same order observed for ΔE_{ads} values, **DES∩B$_{vac}$-h-BNNF**>> **DES∩N$_{vac}$-h-BNNF**> **DES∩h-BNNF**.

To determine the nature of the interaction, we calculated the charge transfer using ChelpG analysis, expressing it as the Q_{CT}, or the value of the charge transfer from the DES to the surfaces as the values are mostly positive suggesting that the surfaces are primarily donating electron density to the solvent rather than vice versa (Table 1).[25] However, the values are low suggesting minimal transfer is occurring. These low values are in line with the limited transfer we observed in our previous study on graphene defects.[6] Binding does however significantly affect the electronics of the surface as can be seen in changes in the HOMO-LUMO gap (Table 2). For the defect free system, the gap falls between 16% and 4%. This follows as the energy of the HOMO falls slightly, and by about the same amount, regardless of the DES. However the energy of the LUMO drops significantly, especially in the case of benzoic acid DES. This leads inevitably and directly to a similar decrease in chemical hardness. For **B$_{vac}$-h-BNNF** the energy gap increases in all cases, again with benzoic acid DES system adopting the lowest LUMO energy (except it is still higher than the nanoflake without the DES). Similarly, chemical hardness rises. Again for **N$_{vac}$-h-BNNF**, the gap falls, but moderately this time, as does, of course chemical hardness. Once again, benzoic acid sees the most significant drop in the LUMO energy.

Table 2. The energy of HOMO (E_{HOMO}) and LUMO (E_{LUMO}) orbitals (in eV), HOMO-LUMO energy gap (E_g in eV) and chemical hardness ($\eta = (E_{LUMO} - E_{HOMO})/2$ in eV) of the surfaces and DES∩surface complexes.

Structure	E_{HOMO}	E_{LUMO}	E_g	η
h-BNNF	-8.10	0.88	8.98	4.49
[ChCl][U]∩h-BNNF	-7.53	0.67	8.20	4.10
[ChCl][Gly]∩h-BNNF	-7.53	0.78	8.31	4.16
[ChCl][EG]∩h-BNNF	-7.76	0.87	8.63	4.32
[ChCl][BA]∩h-BNNF	-7.65	-0.16	7.49	3.75
B_{vac}-h-BNNF	-8.15	-2.05	6.10	3.05
[ChCl][U]∩B_{vac}-h-BNNF	-7.44	0.70	8.14	4.07
[ChCl][Gly]∩B_{vac}-h-BNNF	-7.43	0.28	7.71	3.86
[ChCl][EG]∩B_{vac}-h-BNNF	-7.29	0.70	7.99	4.00
[ChCl][BA]∩B_{vac}-h-BNNF	-7.58	-0.75	6.83	3.42
N_{vac}-h-BNNF	-5.31	0.59	5.90	2.95
[ChCl][U]∩N_{vac}-h-BNNF	-5.37	0.35	5.72	2.86
[ChCl][Gly]∩N_{vac}-h-BNNF	-5.25	0.58	5.83	2.92
[ChCl][EG]∩N_{vac}-h-BNNF	-4.46	0.78	5.24	2.62
[ChCl][BA]∩N_{vac}-h-BNNF	-5.31	-0.18	5.32	2.57

To identify the most important intermolecular interactions, the bond critical points (BCPs) formed between the components of the DESs and the surface were calculated; these results and the QTAIM analysis (in a.u.) at the BCPs are provided as Figure S3 and Table S1, respectively. The magnitude of the electron density ρ(r) values at the BCPs formed between the DESs and the surfaces can be applied to evaluate the strength of the intramolecular interactions in the DES∩surface complexes. The greater the ρ(r) values, the stronger is the intramolecular interactions in the DES∩surface complexes. Our results show that the ρ(r) values at the BCPs of these interactions change from 0.0023 a.u. to 0.1130 a.u. As seen from Table S1, the highest ρ(r) values are seen for the interactions of **[Cl]**$^-$ anion, hydroxyl groups in the **[Ch]**$^+$ cation, **EG**, **Gly**, and the oxygen atom and N-H bonds in the **U** with the B and N atoms in the surfaces. On the other hand, the interaction of **BA** with the surfaces mainly occurs through π-π interactions.

The positive values of Laplacian of electron density, $\nabla^2\rho(r)$, and total energy density, H(r), indicate that the nature of interaction between the surfaces and DESs is primarily noncovalent as expected. However, in some rare cases, the interaction between the nitrogen and boron atoms in the surfaces and oxygen atoms in the DESs are partially covalent and partially electrostatic in nature ($\nabla^2\rho(r)>$

0 and H(r) < 0). They occur between the oxygen of the choline for **[ChCl][U]∩N_{vac}-h-BNNF**, and the boron adjacent to the vacancy. In this case, the hydroxyl proton is participating in a hydrogen bond with the chloride, increasing the local electron density on the oxygen allowing for the interaction. For **[ChCl][U]∩B_{vac}-h-BNNF**, the interaction is between the urea oxygen and a boron adjacent to a nitrogen adjacent to the vacancy. The unusual perpendicularity of the hydroxyl group of **[ChCl][EG]∩N_{vac}-h-BNNF** was noted for providing a stronger than expected interaction. The partial covalent nature of the bond (our QTAIM visualization actually indicates it as a covalent interaction) would certainly help explain the exceptional affinity of this DES. The interaction is with a boron adjacent to the vacancy, and the boron is clearly pulled out of the plane of the nanoflake towards the oxygen (Figure S3, and Figure 1); the induced distortion penalty appears to be easily paid by the benefit of the exceptionally strong interaction. The final semi-covalent interaction is observed for **[ChCl][Gly]∩N_{vac}-h-BNNF** where one of the terminal alcohols of the glycerol donates its hydrogen to the chloride, liberating the required electron density to generate a strong interaction with a nitrogen, distal from the vacancy. Furthermore, our results show that the interactions mentioned above, which are partially covalent and partially electrostatic in the nature have a higher ρ(r) value and thus are stronger than other interactions in the DES∩surface complexes.

In order to evaluate the type and strength of the interactions responsible for adsorption of DESs on the surfaces, the noncovalent interactions (NCIs) of the DES∩surface complexes were determined by plotting the reduced density gradient (RDG) isosurfaces and the RDG isosurfaces versus the sign(λ_2)ρ values (Figure S2). In the NCI plots, the sign(λ_2)×ρ(r) values are negative for the strong attractive interactions such as electrostatic interactions, while they are positive for the steric repulsions. These values are near zero for the van der Waals (vdW) interactions. In addition, the strong attractive interactions such as electrostatic interactions are shown by blue color. The weak interactions such as vdW interactions and strong repulsion interactions such as steric repulsions are specified by green and red colors, respectively. As seen from Figure S2, the negative sign(λ_2)×ρ(r) values in the NCI plots, which show the blue colors are associated with the interaction of hydroxyl group in the **$[Ch]^+$** cation with the **$[Cl]^-$** anion. Hence, these interactions are strong and electrostatic in nature. On the other hand, the green color observed in the NCI plots is associated with the interactions between the DESs and the surfaces, indicates that the adsorption of DESs on the surfaces occurs through weak interactions with the nature of vdW.

3.4. UV-Vis absorption spectra

The final component of our analysis involved applying time dependent DFT (TDDFT) calculations to investigate the effect of DES adsorption on the UV-Vis absorption spectra of the **h-BNNF**, **B_{vac}-h-BNNF**, and **N_{vac}-h-BNNF** surfaces. These are not only potentially optically active materials, but the changes in the optical behaviour reflect underlying shifts in electronics. The absorption spectra of the surfaces and their complexes with the DESs were calculated at the TD-M06-2X/cc-pVDZ level of theory (Figure 3) and characterized by analyzing the optical properties, including main transition configurations, excitation states (n), excitation coefficients, excitation wavelengths (λ), excitation energies (E), and oscillator strengths (f) (Table S2).

The UV-Vis absorption spectrum of the **h-BNNF** surface shows one strong absorption peak at λ = 186 nm, which corresponds to the HOMO→LUMO electronic transition. This observation is in agreement with the results reported by Vovusha et al.[33] They also computationally predicted that **h-BNNF** ($B_{27}N_{27}H_{18}$) surface has a strong absorption peak at λ = 192 nm and a weak shoulder at λ = 184 nm. Furthermore, they also revealed that the absorption peaks are related to the $\pi \rightarrow \pi^*$ electronic transitions (from π orbital of N atom to π^* orbital of B atom). This result is consistent with the calculated absorption energy value of 200 nm found for different sized **h-BNNF** surface.[34] This is also consistent with experimental data that suggests a maximum at approximately 205 nm for extended macro sheets of BN. The longer wavelength would be expected based on the greater conjugation present in larger systems.[35] Other syntheses have prepared material with broad adsorption between 190 and 205.[36]

The creation of B-vacancy and N-vacancy in the **h-BNNF** surface leads to a red-shift of the λ = 186 nm in the **h-BNNF** surface to λ = 304 nm (HOMO-1(β)→LUMO(β)) and λ = 296 nm (HOMO(α)→LUMO+7(α)) in the **B_{vac}-h-BNNF** and **N_{vac}-h-BNNF** surfaces, respectively. Of course, this effect would be averaged out in larger sheets, but in the immediate vicinity of the vacancy, this is likely a reasonable estimation of the drastic effects. In addition, a new peak in the absorption spectrum of **N_{vac}-h-BNNF** surface appears at λ = 421 nm, which corresponds to HOMO(α)→LUMO(α) electronic transition. The presence of B-vacancy in the h-BN surfaces has also been experimentally shown by an absorption peak at 295 nm (4.20 eV).[35]

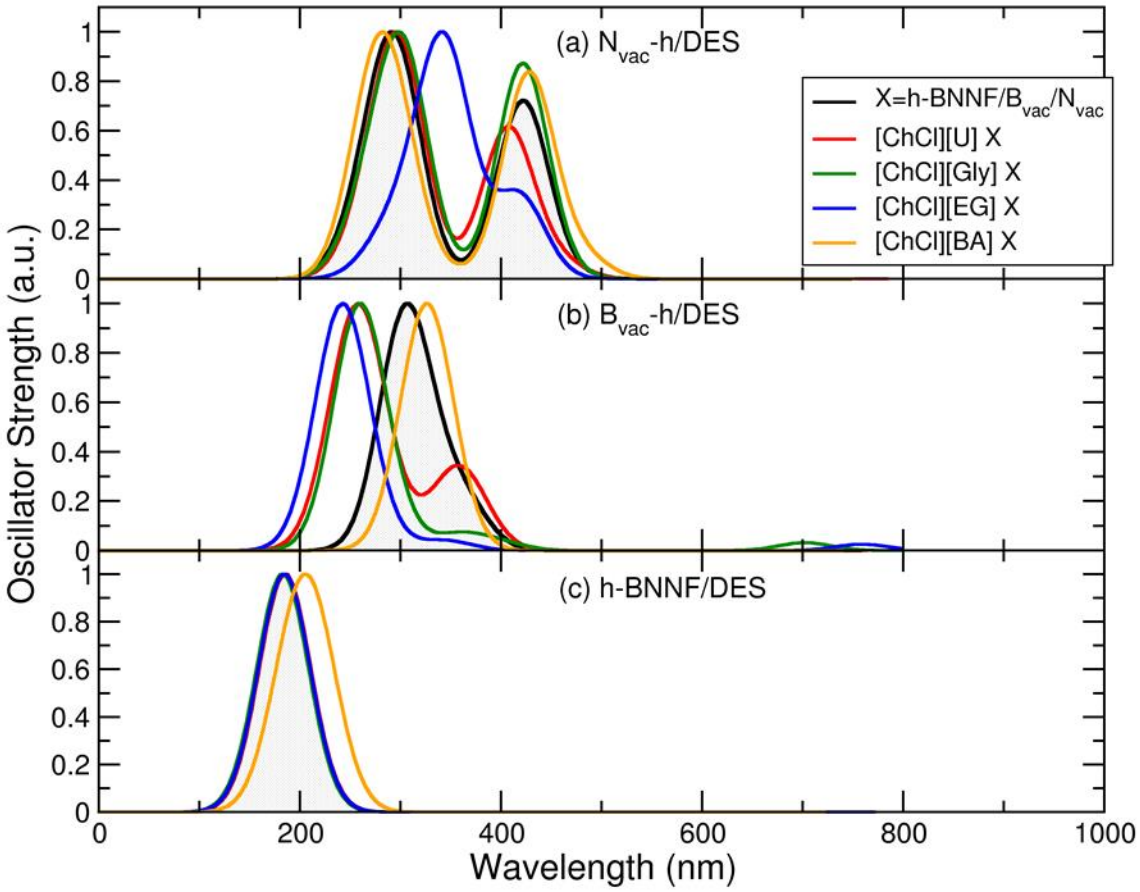

Figure 3. The UV-Vis absorption spectra of **h-BNNF**, **B_{vac}-h-BNNF**, **N_{vac}-h-BNNF** surfaces and their complexes with DESs computed at the TD-M06-2X/cc-pVDZ level of theory.

The TDDFT calculations were also carried out on the DES∩surface complexes to investigate the effect of DES adsorption on the optical properties and absorption spectrum of the surfaces. As seen in Table S2, the absorption spectra of **[ChCl][U]∩h-BNNF**, **[ChCl][Gly]∩h-BNNF**, and **[ChCl][EG]∩h-BNNF** are identical to those of **h-BNNF**, they completely superimpose on the curve of the base nanoflake in Figure 3. Thus, despite the changes noted for this system upon DES binding has no effect on the optical properties of the **h-BNNF** surface. However, a red-shift from λ = 186 nm (HOMO→LUMO) to λ = 214 nm (HOMO-8→LUMO) is observed with adsorption of **[ChCl][BA]** on the **h-BNNF** surface. This DES does adsorb stronger than any of the others, but binding is still weak; the effect may be more due to the negative charge transfer observed for this system due to π interactions with the surface.

Upon adsorption of **[ChCl][U]**, **[ChCl][Gly]** and **[ChCl][EG]** onto the **B_{vac}-h-BNNF** surface, the main absorption peak of this surface at λ = 304 nm (HOMO-1(β)→LUMO(β)) is blue-shifted and new weak absorption peaks appear. In opposition, **[ChCl][BA]** binding to the **B_{vac}-h-BNNF** surface leads to a red-shift of the absorption peak from λ = 304 nm (HOMO-1(β)→LUMO(β)) to λ = 326 nm (HOMO-2(β)→LUMO(β)) but retains the monophasic shape without the appearance of meaningful additional peaks.

Our results revealed that the first absorption peak in the absorption spectrum of **N_{vac}-h-BNNF** at λ = 296 nm (HOMO(α)→LUMO+7(α)) shows a weak red shift upon adsorption of **[ChCl][U]**, **[ChCl][Gly]** and **[ChCl][EG]**, whereas it shows a weak blue shift with adsorption of **[ChCl][BA]**. The second absorption peak at λ = 421 nm (HOMO(α)→LUMO(α)) has a lower intensity than the first absorption peak and also undergoes the same red and blue-shifts with adsorption of DESs to the **N_{vac}-h-BNNF** surface. The greatest shift in the absorption spectra is observed for the adsorption of DESs onto the **B_{vac}-h-BNNF** surface, with the weakest effects on **DES∩h-BNNF**. This is completely consistent with all other calculations that suggest DES binding is strongest to the boron vacant boron nitride.

To determine where the excited electrons involved are moving, the transition density matrix (TDM) heat maps based on the self-defined fragments are used and interpreted based on a self-defined fragment index of electron transfer. In this study, the DES∩surface complexes are divided into three fragments, fragment 1 (**h-BNNF**, **B_{vac}-h-BNNF** or **N_{vac}-h-BNNF**), fragment 2 (**ChCl**), and fragment 3 (HBDs). The fragment TDM heat maps between the ground state and the main excitation states in the complexes are provided as Figure S4 with representative examples included here as Figure 4. The electron density transferred between the surfaces and components of the DESs (**ChCl** and HBDs) in each excitation state are calculated and summarized in Table S3. Furthermore, the iso-surfaces of Rich Martin's natural transition orbital (NTO) pairs[37] for the excitation states in the DES∩surface complexes were calculated and shown in Figure S5. According to the NTO pair theory, electronic transitions occur from the excited particle (occupied) orbital to the empty hole (unoccupied) orbital. It should be mentioned that the use of NTO is much more convenient than employing molecular orbitals for the qualitative description of excitations because the NTO approach produces many fewer orbitals while still providing reliable estimates of the nature of the transition.[37]

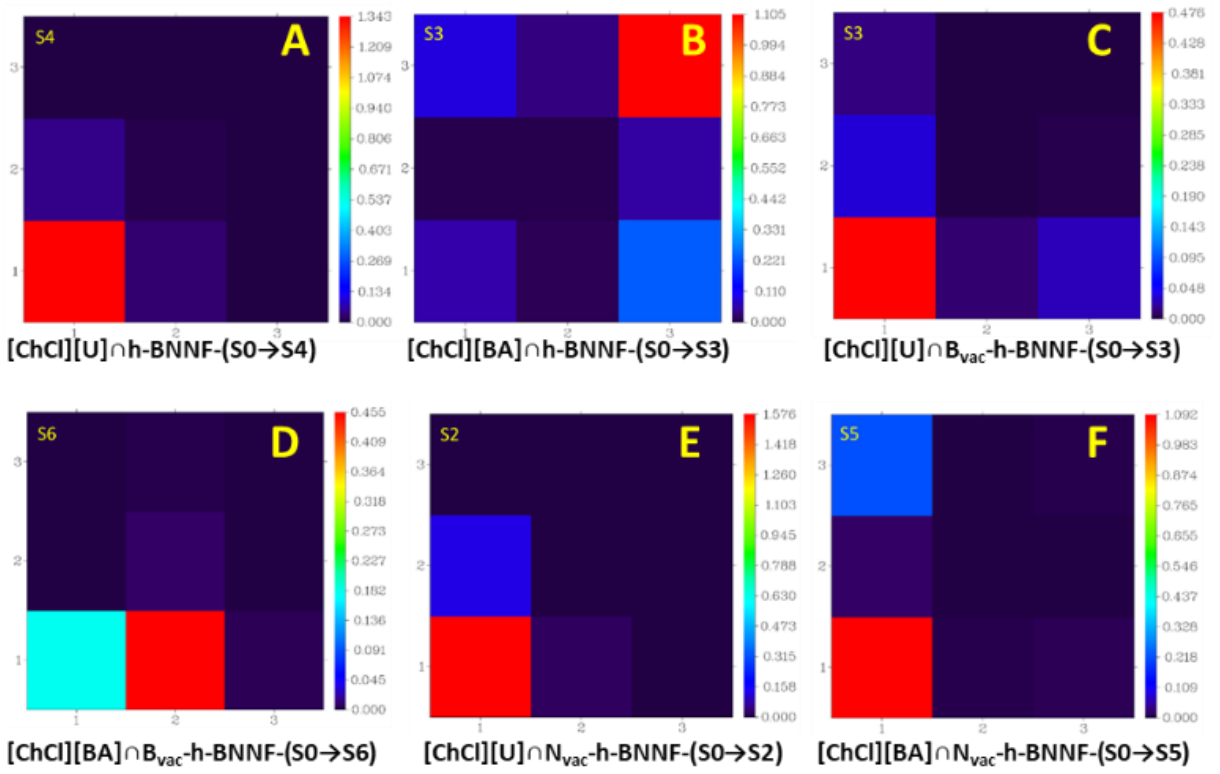

Figure 4. Select transition density matrix maps of the DES∩surface complexes. In these maps, 1, 2 and 3 terms are the surfaces (**h-BNNF**, **B_{vac}-h-BNNF** and **N_{vac}-h-BNNF**), **ChCl** and the HBDs, respectively. All other TDMs are provided as Figure S4. The y axis is the originating fragment, and the x axis is the receiving fragment for the excited electron.

According to the TDM heat maps, the magnitude of the off-diagonal elements (the blue boxes) in the heat maps of the **DES∩h-BNNF** complexes are not significant with respect to their diagonal elements (the red); indicating that there is no meaningful inter fragment electron transfer. Figure 4a is typical of this pattern: all transitions occur within fragment 1. This is to be expected as we see no meaningful change in the optical behaviour of the materials; significant transfer would change the optical spectra.

The electrons and holes are mainly localized on the **h-BNNF** surface (fragment 1) in the **[ChCl][U]∩h-BNNF**, **[ChCl][Gly]∩h-BNNF**, and **[ChCl][EG]∩h-BNNF** complexes. This means that charge transfer following photon absorption for these complexes occurs mainly within the **h-BNNF** surface. However, our results indicate that in these complexes the contribution of charge transfer for the excitation states between the **h-BNNF** surface and **ChCl** is higher than that between the **h-BNNF** surface and HBDs of **U**, **Gly** and **EG** (Table S3). This is indicated in the visual representation by the brighter colour in the (1→2) box than in the 1→3 box. In the case of

[ChCl][BA]∩h-BNNF complex, the NTO pairs indicate that the excited particle (occupied) orbital is distributed on both **h-BNNF** surface (fragment 1) and benzoic acid (BA) (fragment 3), while the empty hole (unoccupied) orbital is only located at the **BA** fragment (Figure S4). According to this result, the TDM heat map of the **[ChCl][BA]∩h-BNNF** complex reveals that the electronic excitation from S0 to S3 in this complex is related to the $\pi \rightarrow \pi^*$ transitions in the benzene aromatic ring in the **BA** molecule (Figure 4b). Additionally, in this complex, the contribution of charge transfer for the excitation state (n = 3) between the **h-BNNF** surface and **BA** molecule is higher than that between the **h-BNNF** surface and **ChCl**. This is all consistent with the other findings above the benzoic acid DES behave differently with the **h-BNNF** than the other systems, and this explains how the presence of the aromatic system affects this interaction.

The values of the off-diagonal elements in the TDM heat maps of the **[ChCl][U]∩B$_{vac}$-h-BNNF**, **[ChCl][Gly]∩B$_{vac}$-h-BNNF**, and **[ChCl][EG]∩B$_{vac}$-h-BNNF** complexes are not significant with respect to their diagonal elements, therefore inter-fragment electron transfer should also not be dominant (Figure 4c). The main feature of the TDM heat maps of these complexes is again related to the local excitation on fragment 1 (**B$_{vac}$-h-BNNF**), which corresponds to the $\pi \rightarrow \pi^*$ transitions. This observation also is confirmed by the NTO pairs shown in Figure S5. In the case of **[ChCl][BA]∩B$_{vac}$-h-BNNF** complex, again the outlier of DES, we can see that the fragment 2 (**ChCl**) has transferred certain amount of electrons to the fragment 1 (**B$_{vac}$-h-BNNF**) because the (1→2) element is large (the red color), and the excited particle orbital and empty hole orbital also simultaneously appear on fragment 1 to some extent (Figure 4d). The NTO pair for the **[ChCl][BA]∩B$_{vac}$-h-BNNF** complex shows that the electronic excitation from S0 to S6 (S0→S6) is mainly related to the electronic transition from lone pairs of **[Cl]$^-$** anion to π^* orbitals of the **B$_{vac}$-h-BNNF** surface and to some extent $\pi \rightarrow \pi^*$ transitions in the **B$_{vac}$-hBNNF** surface. This is unanticipated as it is certainly the case that the chloride anion is well positioned to do so, but it is also more or less equidistant in many of the other complexes already discussed and where this interaction is not observed. In addition, Table S3 indicates that in the **DES∩B$_{vac}$-h-BNNF** complexes the charge transfer for the excitation states between the **B$_{vac}$-h-BNNF** surface and **ChCl** is higher than that between the **B$_{vac}$-h-BNNF** surface and HBDs.

In the **DES∩N$_{vac}$-h-BNNF** complexes, the values of the off-diagonal elements in the TDM maps are not significant with respect to their diagonal elements (Figure 4e). Therefore, electron excitation does not cause a significant charge transfer between the various fragments. The TDM

heat maps in agreement with the NTO pairs reveal that the main feature of electron excitation in these complexes is local excitation on fragment 1 (**N_{vac}-h-BNNF**). Again, the **[ChCl][BA]∩N_{vac}-h-BNNF** system stands out with some transfer from the benzoic acid to the surface (Figure 4f).

4. Conclusions

This study demonstrates that there are substantial differences between the expected adsorption of DES onto defective boron nitride compared with pristine nanoflakes. The predicted binding affinity differences are the biggest changes, and the nature of the defective surface breaking symmetry provides an anchor for the DES to interact. This implies that nanoflakes with a greater proportion of defects should be more "wettable" with DES than purer surfaces. The implications of defects for practical applications remains open as boron nitride science is still in its early stages due to the difficulty of producing this material on scale. However, the presence of defects is not necessarily problematic. In all cases except two, the nature of the surface is more important than the nature of the DES. The two exceptions are benzoic acid DES with the boron vacancy where it doesn't force distortion of the surface leading to its weaker interaction; and ethylene glycol DES with the nitrogen vacancy where the hydroxyl group forms a partially covalent bond with the surface. However, these effects have minimal impact on the charge transfer indicating that any of these solvents might be functionally applicable. The presence of the DES have almost no effect on the optical behaviour of pristine nanoflakes, and although they do shift the λ_{max} of the defective surfaces, these effects are unlikely to be truly meaningful for any practical application with low levels of defects present. Finally, the transitions observed upon photon adsorption for all systems, with only a couple of exceptions, largely occur within the surface. This is desirable as any photoelectric activity or application will want to be focused on the material rather than losing energy to the solvent. In all, this study indicates the DESs are extremely suitable solvents for solvating boron nitride regardless of the defect status, and have little effect on the behaviour of the material.

Author Contributions: Conceptualization: MS-F, GK, JFT, SMT; Funding acquisition: MS-F, HRG, JFT; Investigation: MS-F, SMT, GK, HRG; Methodology: All authors; Supervision: MS-F, JFT; Visualization: GK, SMT; Writing original draft: JFT, SMT; Writing-review and editing: All authors.

Acknowledgements: This research was supported by the Natural Sciences and Engineering Research Council of Canada (2018-06338 to JFT), the American Chemical Society's Petroleum Research Fund (60765-ND7), and the Government of Ontario through an Ontario Early Researcher Award (ER18-14-114 to JFT). SMT and JFT would like to highlight that this work was made possible by the facilities of the Shared Hierarchical Academic Research Computing Network (SHARCNET: www.sharcnet.ca) and Compute/Calcul Canada. MS-F would like to thank Birjand University of Technology for financial support for this work. The authors declare that they have no competing financial interest.

Supporting Information: Additional tables of data, figures, and computational details are available in the accompanying supporting information file.

References

1. Abbott, A. P.; Boothby, D.; Capper, G.; Davies, D. L.; Rasheed, R. K., Deep eutectic solvents formed between choline chloride and carboxylic acids: Versatile alternatives to ionic liquids. *J. Am. Chem. Soc.* **2004,** *126* (29), 9142-9147. DOI: 10.1021/ja048266j

2. (a) Abo-Hamad, A.; Hayyan, M.; AlSaadi, M. A.; Hashim, M. A., Potential applications of deep eutectic solvents in nanotechnology. *Chem. Eng. J. (Amsterdam, Neth.)* **2015,** *273*, 551-567. DOI: https://doi.org/10.1016/j.cej.2015.03.091 ; (b) Chakrabarti, M. H.; Mjalli, F. S.; AlNashef, I. M.; Hashim, M. A.; Hussain, M. A.; Bahadori, L.; Low, C. T. J., Prospects of applying ionic liquids and deep eutectic solvents for renewable energy storage by means of redox flow batteries. *Renewable Sustainable Energy Rev.* **2014,** *30*, 254-270. DOI: https://doi.org/10.1016/j.rser.2013.10.004 ; (c) Cvjetko Bubalo, M.; Vidović, S.; Radojčić Redovniković, I.; Jokić, S., Green solvents for green technologies. *Journal of Chemical Technology & Biotechnology* **2015,** *90* (9), 1631-1639. DOI: 10.1002/jctb.4668 ; (d) Jhong, H.-R.; Wong, D. S.-H.; Wan, C.-C.; Wang, Y.-Y.; Wei, T.-C., A novel deep eutectic solvent-based ionic liquid used as electrolyte for dye-sensitized solar cells. *Electrochem. Commun.* **2009,** *11* (1), 209-211. DOI: https://doi.org/10.1016/j.elecom.2008.11.001 ; (e) Mbous, Y. P.; Hayyan, M.; Hayyan, A.; Wong, W. F.; Hashim, M. A.; Looi, C. Y., Applications of deep eutectic solvents in biotechnology and bioengineering—Promises and challenges. *Biotechnol. Adv.* **2017,** *35* (2), 105-134. DOI: https://doi.org/10.1016/j.biotechadv.2016.11.006 ; (f) Paiva, A.; Craveiro, R.; Aroso, I.; Martins, M.; Reis, R. L.; Duarte, A. R. C., Natural deep eutectic solvents – Solvents for the 21st Century. *ACS Sustainable Chem. Eng.* **2014,** *2* (5), 1063-1071. DOI: 10.1021/sc500096j ; (g) Radošević, K.; Cvjetko Bubalo, M.; Gaurina Srček, V.; Grgas, D.; Landeka Dragičević, T.; Radojčić Redovniković, I., Evaluation of toxicity and biodegradability of choline chloride based deep eutectic solvents. *Ecotoxicol. Environ. Saf.* **2015,** *112*, 46-53. DOI: https://doi.org/10.1016/j.ecoenv.2014.09.034 ; (h) Smith, E. L.; Abbott, A. P.; Ryder, K. S., Deep eutectic solvents (DESs) and their applications. *Chem. Rev.* **2014,** *114* (21), 11060-11082. DOI: 10.1021/cr300162p

3. (a) Chakrabarti, M. H.; Manan, N. S. A.; Brandon, N. P.; Maher, R. C.; Mjalli, F. S.; AlNashef, I. M.; Hajimolana, S. A.; Hashim, M. A.; Hussain, M. A.; Nir, D., One-pot electrochemical gram-scale synthesis of graphene using deep eutectic solvents and acetonitrile. *Chem. Eng. J. (Amsterdam, Neth.)* **2015,** *274*, 213-223. DOI: http://doi.org/10.1016/j.cej.2015.03.083 ; (b) Abdelkader, A. M.; Patten, H. V.; Li, Z.; Chen, Y.; Kinloch, I. A., Electrochemical exfoliation of graphite in quaternary ammonium-based deep eutectic solvents: A route for the mass production of graphane. *Nanoscale* **2015,** *7* (26), 11386-11392. DOI: http://doi.org/10.1039/C5NR02840J ; (c) Hayyan, M.; Abo-Hamad, A.; AlSaadi, M. A.; Hashim, M. A., Functionalization of graphene using deep eutectic solvents. *Nanoscale Res. Lett.* **2015,** *10* (1), 324. DOI: http://doi.org/10.1186/s11671-015-1004-2 ; (d) Wang, X.; Li, G.; Row, K. H., Graphene and graphene oxide modified by deep eutectic solvents and ionic liquids supported on silica as adsorbents for solid-phase extraction. *Bull. Korean Chem. Soc.* **2017,** *38* (2), 251-257. DOI: http://doi.org/10.1002/bkcs.11074

4. Sun, H.; Li, Y.; Wu, X.; Li, G., Theoretical study on the structures and properties of mixtures of urea and choline chloride. *J. Mol. Model.* **2013,** *19* (6), 2433-2441. DOI: http://doi.org/10.1007/s00894-013-1791-2

5. (a) Mamme, M. H.; Moors, S. L. C.; Terryn, H.; Deconinck, J.; Ustarroz, J.; De Proft, F., Atomistic insight into the electrochemical double layer of choline chloride–Urea deep eutectic solvents: Clustered interfacial structuring. *J. Phys. Chem. Lett.* **2018,** *9* (21), 6296-6304. DOI: http://doi.org/10.1021/acs.jpclett.8b01718 ; (b) Atilhan, M.; Aparicio, S., Molecular dynamics simulations of mixed deep eutectic solvents and their interaction with nanomaterials. *J. Mol. Liq.* **2019,** *283*, 147-154. DOI: http://doi.org/10.1016/j.molliq.2019.03.068 ; (c) Atilhan, M.; Aparicio, S., Deep eutectic solvents on the surface of face centered cubic metals. *J. Phys. Chem. C* **2016,** *120* (19), 10400-10409. DOI: http://doi.org/10.1021/acs.jpcc.6b01826 ; (d) Atilhan, M.; Costa, L. T.; Aparicio, S., Elucidating the properties of graphene–deep eutectic solvents interface. *Langmuir* **2017,** *33* (21), 5154-5165. DOI: http://doi.org/10.1021/acs.langmuir.7b00767 ; (e) Rozas, S.; Atilhan, M.; Aparicio, S., Deep eutectic solvent Reline at 2D nanomaterial interfaces. *J. Phys. Chem. B* **2020,** *124* (7), 1197-1206. DOI: http://doi.org/10.1021/acs.jpcb.9b08873

6. Shakourian-Fard, M.; Taimoory, S. M.; Ghenaatian, H. R.; Kamath, G.; Trant, J. F., A DFT study of the adsorption of deep eutectic solvents onto graphene and defective graphene nanoflakes. *J. Mol. Liq.* **2021,** *327*, 114850. DOI: http://doi.org/10.1016/j.molliq.2020.114850

7. (a) Zhang, J.; Sun, R.; Ruan, D.; Zhang, M.; Li, Y.; Zhang, K.; Cheng, F.; Wang, Z.; Wang, Z.-M., Point defects in two-dimensional hexagonal boron nitride: A perspective. *J. Appl. Phys.* **2020,** *128* (10), 100902. DOI: http://doi.org/10.1063/5.0021093 ; (b) Lale, A.; Bernard, S.; Demirci, U. B., Boron nitride for hydrogen storage. *ChemPlusChem* **2018,** *83* (10), 893-903. DOI: http://doi.org/10.1002/cplu.201800168 ; (c) Golberg, D.; Bando, Y.; Tang, C. C.; Zhi, C. Y., Boron nitride nanotubes. *Adv. Mater. (Weinheim, Ger.)* **2007,** *19* (18), 2413-2432. DOI: 10.1002/adma.200700179

8. Ma, R.; Bando, Y.; Zhu, H.; Sato, T.; Xu, C.; Wu, D., Hydrogen uptake in boron nitride nanotubes at room temperature. *J. Am. Chem. Soc.* **2002,** *124* (26), 7672-7673. DOI: http://doi.org/10.1021/ja026030e

9. (a) Bhatia, S. K.; Myers, A. L., Optimum conditions for adsorptive storage. *Langmuir* **2006,** *22* (4), 1688-1700. DOI: http://doi.org/10.1021/la0523816 ; (b) Dillon, A. C.; Heben, M. J., Hydrogen storage using carbon adsorbents: Past, present and future. *Appl. Phys. A* **2001,** *72* (2), 133-142. DOI: http://doi.org/10.1007/s003390100788

10. Noura, M.; Rahdar, A.; Taimoory, S. M.; Hayward, J. J.; Sadraei, S. I.; Trant, J. F., Effect of aluminium-doped boron-nitride nanotube architecture on hydrogen adsorption: A first-principles DFT examination. *Int. J. Hydrog. Energy* **2020,** *45*, 11176-11189. DOI: http://doi.org/10.1016/j.ijhydene.2020.02.053

11. Wang, Q.; Zhang, Q.; Zhao, X.; Luo, X.; Wong, C. P. Y.; Wang, J.; Wan, D.; Venkatesan, T.; Pennycook, S. J.; Loh, K. P.; Eda, G.; Wee, A. T. S., Photoluminescence upconversion by defects in hexagonal boron nitride. *Nano Lett.* **2018,** *18* (11), 6898-6905. DOI: http://doi.org/10.1021/acs.nanolett.8b02804
12. Huang, B.; Xiang, H.; Yu, J.; Wei, S.-H., Effective control of the charge and magnetic states of transition-metal atoms on single-layer boron nitride. *Phys. Rev. Lett.* **2012,** *108* (20), 206802. DOI: http://doi.org/10.1103/PhysRevLett.108.206802
13. Krivanek, O. L.; Chisholm, M. F.; Nicolosi, V.; Pennycook, T. J.; Corbin, G. J.; Dellby, N.; Murfitt, M. F.; Own, C. S.; Szilagyi, Z. S.; Oxley, M. P.; Pantelides, S. T.; Pennycook, S. J., Atom-by-atom structural and chemical analysis by annular dark-field electron microscopy. *Nature* **2010,** *464* (7288), 571-574. DOI: http://doi.org/10.1038/nature08879
14. Pham, T.; Gibb, A. L.; Li, Z.; Gilbert, S. M.; Song, C.; Louie, S. G.; Zettl, A., Formation and dynamics of electron-irradiation-induced defects in hexagonal boron nitride at elevated temperatures. *Nano Lett.* **2016,** *16* (11), 7142-7147. DOI: http://doi.org/10.1021/acs.nanolett.6b03442
15. Shakourian-Fard, M.; Jamshidi, Z.; Bayat, A.; Kamath, G., Meta-hybrid density functional theory study of adsorption of imidazolium- and ammonium-based ionic liquids on graphene sheet. *J. Phys. Chem. C* **2015,** *119* (13), 7095-7108. DOI: http://doi.org/10.1021/jp512020q
16. Shakourian-Fard, M.; Kamath, G., The effect of defect types on the electronic and optical properties of graphene nanoflakes physisorbed by ionic liquids. *Phys. Chem. Chem. Phys.* **2017,** *19* (6), 4383-4395. DOI: http://doi.org/10.1039/C6CP07455C
17. Shakourian-Fard, M.; Ghenaatian, H. R.; Kamath, G.; Taimoory, S. M., Unraveling the effect of nitrogen doping on graphene nanoflakes and the adsorption properties of ionic liquids: A DFT study. *J. Mol. Liq.* **2020,** *312*, 113400. DOI: http://doi.org/10.1016/j.molliq.2020.113400
18. Shakourian-Fard, M.; Kamath, G.; Jamshidi, Z., Trends in physisorption of ionic liquids on boron-nitride sheets. *J. Phys. Chem. C* **2014,** *118* (45), 26003-26016. DOI: http://doi.org/10.1021/jp506277n
19. (a) Shakourian-Fard, M.; Bayat, A.; Kamath, G., Effect of mono-vacant defects on the opto-electronic properties of ionic liquid functionalized hexagonal boron-nitride nanosheets. *J. Mol. Liq.* **2018,** *249*, 1172-1182. DOI: http://doi.org/10.1016/j.molliq.2017.11.140 ; (b) Talaei, R.; Khalili, B.; Mokhtary, M., Modulation of opto-electronic properties of the functionalized hexagonal boron nitride nanosheets with tunable aryl alkyl ionic liquids (TAAILs): Defect based analysis. *J. Mol. Liq.* **2020,** *304*, 112696. DOI: http://doi.org/10.1016/j.molliq.2020.112696
20. Zhao, Y.; Truhlar, D. G., The M06 suite of density functionals for main group thermochemistry, thermochemical kinetics, noncovalent interactions, excited states, and transition elements: two new functionals and systematic testing of four M06-class functionals and 12 other functionals. *Theoretical Chemistry Accounts* **2008,** *120* (1), 215-241. DOI: 10.1007/s00214-007-0310-x
21. Zhao, Y.; Schultz, N. E.; Truhlar, D. G., Design of density functionals by combining the method of constraint satisfaction with parametrization for thermochemistry, thermochemical kinetics, and noncovalent interactions. *J. Chem. Theory Comput.* **2006,** *2* (2), 364-382. DOI: http://doi.org/10.1021/ct0502763
22. Grimme, S.; Antony, J.; Ehrlich, S.; Krieg, H., A consistent and accurate ab initio parametrization of density functional dispersion correction (DFT-D) for the 94 elements H-Pu. *J Chem. Phys.* **2010,** *132* (15), 154104. DOI: http://doi.org/10.1063/1.3382344
23. Frisch, M. J.; Trucks, G. W.; Schlegel, H. B.; Scuseria, G. E.; Robb, M. A.; Cheeseman, J. R.; Scalmani, G.; Barone, V.; Mennucci, B.; Petersson, G. A.; Nakatsuji, H.; Caricato, M.; Li, X.; Hratchian, H. P.; Izmaylov, A. F.; Bloino, J.; Zheng, G.; Sonnenberg, J. L.; Hada, M.; Ehara, M.; Toyota, K.; Fukuda, R.; Hasegawa, J.; Ishida, M.; Nakajima, T.; Honda, Y.; Kitao, O.; Nakai, H.; Vreven, T.; Montgomery Jr., J. A.; Peralta, J. E.; Ogliaro, F.; Bearpark, M. J.; Heyd, J.; Brothers, E. N.; Kudin, K. N.; Staroverov, V. N.; Kobayashi, R.; Normand, J.; Raghavachari, K.; Rendell, A. P.; Burant, J. C.; Iyengar, S. S.; Tomasi, J.; Cossi,

M.; Rega, N.; Millam, N. J.; Klene, M.; Knox, J. E.; Cross, J. B.; Bakken, V.; Adamo, C.; Jaramillo, J.; Gomperts, R.; Stratmann, R. E.; Yazyev, O.; Austin, A. J.; Cammi, R.; Pomelli, C.; Ochterski, J. W.; Martin, R. L.; Morokuma, K.; Zakrzewski, V. G.; Voth, G. A.; Salvador, P.; Dannenberg, J. J.; Dapprich, S.; Daniels, A. D.; Farkas, Ö.; Foresman, J. B.; Ortiz, J. V.; Cioslowski, J.; Fox, D. J. *Gaussian 09*, Gaussian, Inc.: Wallingford, CT, USA, 2009.

24. Boys, S. F.; Bernardi, F., The calculation of small molecular interactions by the differences of separate total energies. Some procedures with reduced errors. *Mol. Phys.* **1970,** *19* (4), 553-566. DOI: http://doi.org/10.1080/00268977000101561

25. Breneman, C. M.; Wiberg, K. B., Determining atom-centered monopoles from molecular electrostatic potentials. The need for high sampling density in formamide conformational analysis. *J. Comput. Chem.* **1990,** *11* (3), 361-373. DOI: http://doi.org/10.1002/jcc.540110311

26. Bader, R. F. W., *Atoms in molecules, a quantum theory*. Oxford Univeristy Press: Oxford, 1990. DOI:

27. Biegler-Konig, F.; Schonbohm, J.; Bayles, D., AIM2000. *J. Comput. Chem.* **2001,** *22* (5), 545-559. DOI: http://doi.org/10.1002/1096-987x(20010415)22:5<545::aid-jcc1027>3.0.co;2-y

28. Lu, T.; Chen, F., Multiwfn: A multifunctional wavefunction analyzer. *J. Comput. Chem.* **2011,** *33* (5), 580-592. DOI: http://doi.org/10.1002/jcc.22885

29. Humphrey, W.; Dalke, A.; Schulten, K., VMD: Visual molecular dynamics. *J. Mol. Graph.* **1996,** *14* (1), 33-38. DOI: http://doi.org/10.1016/0263-7855(96)00018-5

30. Parr, R. G.; Pearson, R. G., Absolute hardness: Companion parameter to absolute electronegativity. *J. Am. Chem. Soc* **1983,** *105* (26), 7512-7516. DOI: http://doi.org/10.1021/ja00364a005

31. (a) Mohan, N.; Suresh, C. H.; Kumar, A.; Gadre, S. R., Molecular electrostatics for probing lone pair–π interactions. *Phys. Chem. Chem. Phys.* **2013,** *15* (42), 18401-18409. DOI: http://doi.org/10.1039/C3CP53379D ; (b) Gadre, S.; Shirsat, R. N. In *Electrostatics of Atoms and Molecules*, 2001; (c) Politzer, P.; Murray, J. S., The fundamental nature and role of the electrostatic potential in atoms and molecules. *Theor. Chem. Acc.* **2002,** *108* (3), 134-142. DOI: http://doi.org/10.1007/s00214-002-0363-9

32. Alizadeh, V.; Malberg, F.; Pádua, A. A. H.; Kirchner, B., Are there magic compositions in deep eutectic solvents? Effects of composition and water content in choline chloride/ethylene glycol from *Ab Initio* molecular dynamics. *J. Phys. Chem. B* **2020,** *124* (34), 7433-7443. DOI: http://doi.org/10.1021/acs.jpcb.0c04844

33. Vovusha, H.; Sanyal, B., DFT and TD-DFT studies on the electronic and optical properties of explosive molecules adsorbed on boron nitride and graphene nano flakes. *RSC Adv.* **2015,** *5* (6), 4599-4608. DOI: http://doi.org/10.1039/C4RA11314D

34. Sanyal, S.; Manna, A. K.; Pati, S. K., BN-decorated graphene nanoflakes with tunable opto-electronic and charge transport properties. *J. Mater. Chem. C* **2014,** *2* (16), 2918-2928. DOI: http://doi.org/10.1039/C3TC32486A

35. Kumbhakar, P.; Kole, A. K.; Tiwary, C. S.; Biswas, S.; Vinod, S.; Taha-Tijerina, J.; Chatterjee, U.; Ajayan, P. M., Nonlinear optical properties and temperature-dependent UV–Vis absorption and photoluminescence emission in 2D hexagonal boron nitride nanosheets. *Adv. Opt. Mater.* **2015,** *3* (6), 828-835. DOI: http://doi.org/10.1002/adom.201400445

36. Li, Q.; Zhang, Q.; Bai, Y.; Zhang, H.; Hu, P.; Li, Y.; Yun, F., Deep-UV hexagonal boron nitride (hBN)/BAlN distributed Bragg reflectors fabricated by RF-sputtering. *Optical Materials Express* **2021,** *11* (1), 180-188. DOI: http://doi.org/10.1364/OME.414330

37. Martin, R. L., Natural transition orbitals. *J. Chem. Phys.* **2003,** *118* (11), 4775-4777. DOI: http://doi.org/10.1063/1.1558471